Shock Waves
DOI 10.1007/s00193-008-0160-z

ORIGINAL ARTICLE

Supersonic flow separation in planar nozzles

Dimitri Papamoschou · Andreas Zill · Andrew Johnson

Received: 15 February 2008 / Accepted: 8 July 2008

Abstract We present experimental results on separation of supersonic flow inside a convergent–divergent (CD) nozzle. The study is motivated by the occurrence of mixing enhancement outside CD nozzles operated at low pressure ratio. A novel apparatus allows investigation of many nozzle geometries with large optical access and measurement of wall and centerline pressures. The nozzle area ratio ranged from 1.0 to 1.6 and the pressure ratio ranged from 1.2 to 1.8. At the low end of these ranges, the shock is nearly straight. As the area ratio and pressure ratio increase, the shock acquires two lambda feet. Towards the high end of the ranges, one lambda foot is consistently larger than the other and flow separation occurs asymmetrically. Downstream of the shock, flow accelerates to supersonic speed and then recompresses. The shock is unsteady, however, there is no evidence of resonant tones. The separation shear layer on the side of the large lambda foot exhibits intense instability that grows into large eddies near the nozzle exit. Time-resolved wall pressure measurements indicate that the shock oscillates in a piston-like manner and most of the energy of the oscillations is at low frequency.

Keywords Supersonic nozzle flow separation · Oscillating shock · Flow instability

PACS 47.40.-x · 47.40.Nm · 47.32.Ff

Communicated by H. Olivier and A. Hadjadj.

D. Papamoschou (✉) · A. Johnson
University of California, Irvine, CA, USA
e-mail: dpapamos@uci.edu

A. Zill
Pankl Aerospace Systems, Cerritos, CA, USA

1 Introduction

Separation of supersonic flow in a convergent–divergent nozzle is a basic fluid-dynamics phenomenon that occurs in a variety of aerospace applications. When a supersonic nozzle is operating at pressure ratios well below its design point, a shock forms inside the nozzle and flow downstream of the shock separates from the nozzle walls. Even though this flow is very basic, it remains poorly understood. This is illustrated by the large discrepancy between predictions of quasi-one-dimensional inviscid theory and the actual behavior of the flow, as will be shown in this paper. Even though separation is typically viewed as an undesirable occurrence, it may have some interesting applications in the area of fluid mixing. Specifically, past work at U.C. Irvine has shown that flow exiting a severely-overexpanded nozzle exhibits a strong instability that enhances mixing of the flow itself and of an adjacent flow. The resulting method of Mixing Enhancement via Secondary Parallel Injection (MESPI) has been proven in a variety of circular and rectangular nozzles [1–3]. Figure 1 shows an example application in a round jet. The physical mechanisms behind this method remain obscure, hence the need to study the fundamental fluid mechanics of supersonic nozzle flow separation.

Supersonic nozzle flow separation occurs in convergent-divergent nozzles subjected to pressure ratios much below their design value, resulting in shock formation inside the nozzle. In the one-dimensional, inviscid treatment of Fig. 2a, the shock is normal and the flow past the shock stays attached to the wall, thus compresses subsonically to the ambient static pressure. In reality, flow detaches and forms a separation region near the wall, as depicted in Fig. 2b. For moderate nozzle area ratios a lambda shock is often observed. Flow downstream of the shock is non-uniform and its structure is very complex.

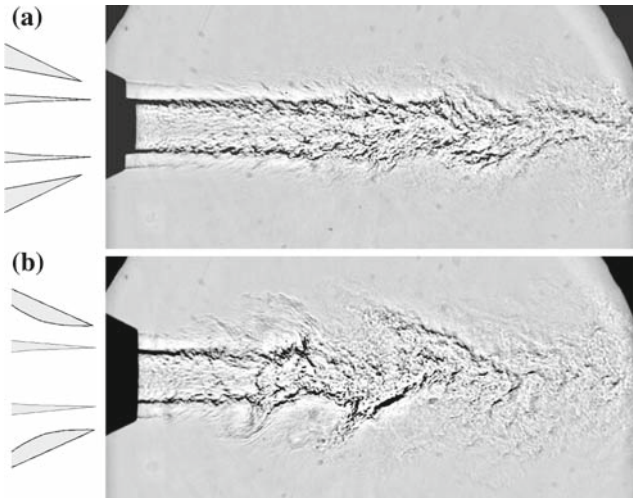

Fig. 1 Primary jet flow at Mach 0.9 surrounded by an annular secondary flow at nozzle pressure ratio NPR = 1.7. **a** Secondary nozzle is convergent, **b** secondary nozzle is convergent–divergent

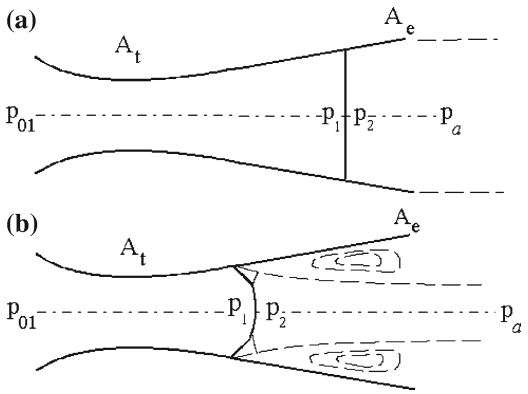

Fig. 2 Sketch of shock structure and fluid phenomena for overexpanded nozzle. **a** Inviscid case, **b** viscous (separated) case

There is a large volume of literature dealing with separation in rocket nozzles, which have large expansion ratios. A paramount issue is prediction of separation location, specifically the ratio p_s/p_a (pressure just ahead of separation over ambient pressure). A review of the older literature and compilation of experimental results in a large variety of nozzles is given by Morrisette and Goldberg [4]. Their primary conclusion is that zero-pressure-gradient separation predictors, like the method of Reshotko and Tucker [5], give reasonable predictions for nozzles with turbulent separation and large divergence angles. The ratio p_s/p_a is a declining function of the shock Mach number M_s and, as a rule of thumb, is roughly 0.5 for $M_s \approx 2$ and 0.3 for $M_s \approx 4$. Nozzles with laminar separation exhibited higher separation pressure ratios. Separation in nozzles with low local wall angles, such as low-divergence conical nozzles and contoured nozzles, deviated from the above predictions. The close proximity of the wall to the separation shear layer has been cited as a possible reason for the discrepancy.

Computational studies of two-dimensional overexpanded nozzles by Wilmoth and Leavitt [6] and by Hamed and Voyatzis [7,8] assessed the accuracy of turbulence models for predicting the flow field and thrust performance. The works agree on the basic structure of the separation shock, which consists of the incident shock, Mach stem (normal shock), and reflected shock. Thrust predictions were in good agreement with experiments, except at pressure ratios associated with separated flow. A combined experimental and computational work by Hunter [9] offers one of the most comprehensive treatments of this flow. His experimental results on a two-dimensional nozzle with $A_e/A_t = 1.8$ showed two distinct separation regimes: three-dimensional separation with partial reattachment for nozzle pressure ratio NPR $\leq$ 1.8 and fully detached two-dimensional separation for NPR $\geq$ 2.0. Hunter claims that this transition was not the result of markedly different onset conditions or stronger shock-boundary layer interaction, but instead came about trough the natural tendency of an overexpanded nozzle flow to detach and reach a more efficient thermodynamic balance. As a result, the thrust of the separated case is much higher than that given by inviscid analysis. Notable in Hunter's experiments and simulations was the much higher nozzle pressure ratio required to situate the shock at a given area ratio compared to the inviscid prediction. For example, to place the normal shock just outside the nozzle exit, a nozzle pressure ratio NPR = 3.4 was required, versus NPR = 1.8 predicted in the inviscid case.

Generic methods for boundary-layer separation cannot capture the entirety of events inside a nozzle. Recently, a theoretical model proposed by Romine [10] fills this gap. For shocks with moderate Mach numbers (less than 2.25), Romine postulates that the jet flow emerging from the shock is above ambient pressure and adjusts to the ambient pressure via a gradual underexpansion. The magnitude of the underexpansion is equal to that of the overall overexpansion. It is important to note that this argument applies in the vicinity of the *centerline* of the nozzle, where the shock is normal, and not on the walls. On the walls, Romine postulates that flow adjusts to the ambient pressure almost immediately past the shock. The underexpansion is evident in the computational Mach number contours of Hunter [9], although he did not mention it explicitly.

An interesting phenomenon related to supersonic nozzle flow separation is that of "aeroacoustic resonance," studied by Zaman et al. [11]. It occurs often, but not always, in convergent-divergent nozzles operated at low pressure ratios, and is characterized by strong acoustic tones and their harmonics. The work by Zaman et al. connected the tone generation to the unsteadiness of the shock system and showed that the frequencies scale with the distance from the shock foot to the nozzle exit. Tripping the nozzle's internal boundary layer

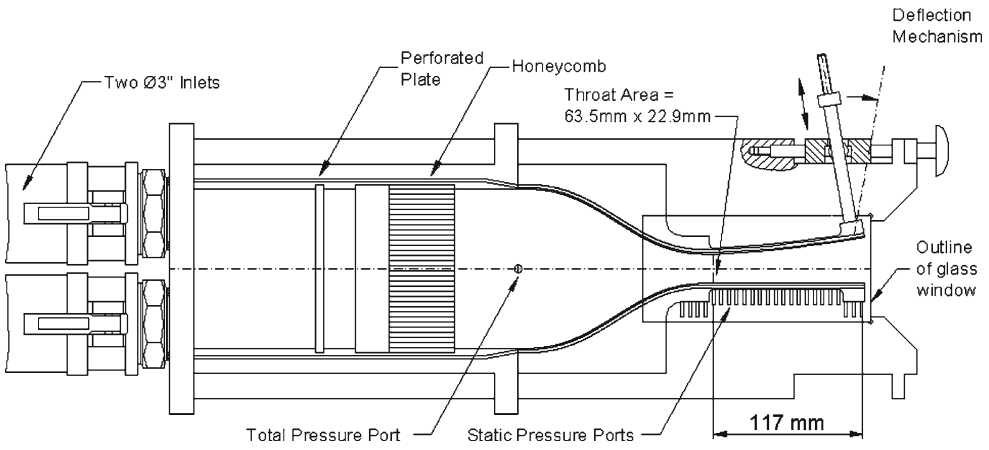

Fig. 3 Schematic of variable nozzle apparatus

suppresses the tones. Aeroacoustic resonance was an early suspect mechanism for the MESPI phenomenon. However, it was largely ruled out because mixing enhancement persisted with or without resonant tones [12].

This paper focuses on the gas dynamic phenomena inside the nozzle and integrates results obtained in a series of experiments [13,14] conducted in a facility specially designed for the study of supersonic nozzle flow separation.

2 Experiment

It was desired to study nozzle separation in an apparatus that afforded flexibility in wall geometry and optical diagnostic access. Accordingly, a novel facility, shown in Fig. 3, was constructed. The upper and lower walls of the nozzle consist of flexible plates that can assume a variety of shapes. Nozzle shaping is achieved by actuators, mounted at the end of each plate, that control the transverse force and moment applied at the end of each plate. This mechanism allows variations of the nozzle area ratio, nozzle contour, and maximum wall angle. Investigation of "half-nozzles" is also possible by deflecting only one of the plates. The nominal test section dimensions are 22.9 mm in height, 63.5 mm in width, and 117 mm in length from throat to exit. The sidewalls of the nozzle incorporate large optical windows for visualization of the entire internal flow, from the subsonic converging section to the nozzle exit. The apparatus is connected to a system that delivers pressure-regulated air and air mixed with either helium or argon. The use of variable-density gas is primarily a means of controlling the Reynolds number and specific heat ratio. The facility is designed for a maximum nozzle pressure ratio (NPR $= p_{0_1}/p_a$) of 3.5, which allows investigation of the entire sequence of internal events (from subsonic flow, to flow with shocks, to shock-free flow) in nozzles with exit-to-throat area ratios up to 1.60.

In the study reported here, the nozzle walls were diverged symmetrically by applying force only (no moment) on the actuators. Consequently, each wall assumed the shape of a cantilevered beam with point force applied to its end, and the nozzle was "trumpet-shaped" with the wall angle increasing monotonically from throat to exit. The exit-to-throat area ratio, A_e/A_t ranged from 1.0 to 1.6. Pure air was supplied at nozzle pressure ratio (NPR $= p_{0_1}/p_a$) ranging from 1.2 to 1.8, corresponding to fully expanded Mach numbers from 0.52 to 0.96. For the convergent–divergent configurations, the Reynolds number based on throat height ranged from to 4.2×10^5 (NPR $= 1.2$) to 6.4×10^5 (NPR $= 1.8$). Diagnostic tools for this study consisted of spark schlieren photography of the internal and external flow; wall pressure measurement; and nozzle centerline pressure measurement.

The Schlieren system employed a 20-nanosecond spark as a light source (Xenon, Model N787), lenses with 150-mm diameter and 1-m focal length for collimating the beam, and a charged coupled device (CCD) camera for acquiring the images (Photometrics, Star 1). The spatial resolution of the images was 576 × 384 pixels.

The upper and lower wall each incorporate 24 static pressure ports that are equally spaced in the axial direction and are arranged along the midwidth of the nozzle. Each row of ports starts upstream of the nozzle throat, at area ratio $A/A_t = 1.14$, and ends at the nozzle exit. The diameter of each port on the surface of the nozzle is 0.8 mm. The nozzle wall ports were scanned by a mechanical pressure multiplexer (Scanivalve, Model SSS-48), which consists of a pneumatic selector switch connected to a single pressure transducer (Setra, Model 280). The use of a single transducer simplified calibration and thus increases the reliability of the pressure measurement. For the experiments reported here, the scan rate was 3 ports per second.

The static pressure along the centerline of the nozzle and jet plume was measured by a 0.5-mm static port drilled into

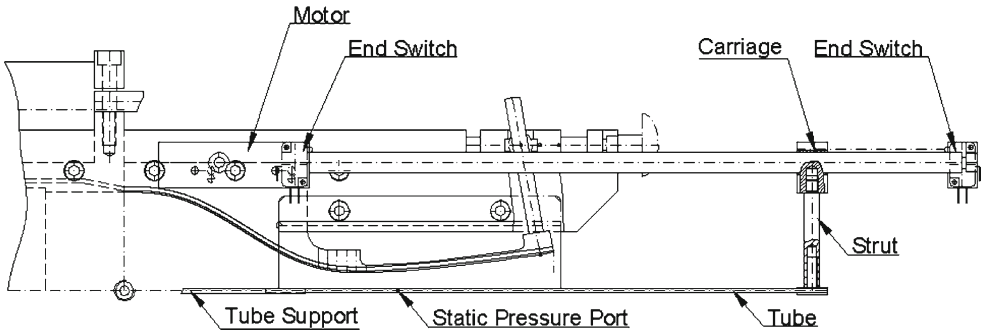

Fig. 4 Schematic of centerline static pressure measurement system

a 2.4-mm-diameter strainless-steel tube that was translated axially along the nozzle. See Fig. 4 for the centerline pressure measurement system. The upstream end of the tube was capped and the downstream end was connected to a pressure transducer (Setra, Model 280). The upstream end of the tube was supported by the honeycomb flow straightener, thus did not introduce any appreciable disturbance into the flow. The downstream end was attached to streamlined strut placed far from the nozzle exit. The strut and tube assembly was translated by a motorized linear actuation stage mounted on the nozzle structure but placed completely outside the jet flow. The orifice in the steel tube traveled from 24 mm upstream of the nozzle throat to 20 mm downstream of the nozzle exit. The tube occupied 0.3% of the nominal nozzle cross sectional area of the nozzle, and the flow deflection it caused (due to boundary layer formation on the tube) was extremely small. Thus, the presence of the tube in the test section did not change the flow phenomena inside and outside the nozzle. A similar method was used circa 1903 by Stodola [15] to measure the centerline pressure distribution in an axisymmetric Laval nozzle.

Time-resolved wall pressure measurements were obtained using two Endevco Model 8507C-15 piezoresistive transducers flush mounted on the upper and lower walls, as shown in Fig. 5. The transducers were located at a distance of 63.5 mm from the throat on the centerline of each wall. For each experimental run, the two transducers were sampled simultaneously each at a sampling rate of 100 kHz for a duration of 1 s. The Nyquist frequency is thus 50 kHz, but avoidance of the transducer resonance sets the useful frequency limit to 30 kHz. Auto-spectra and cross-spectra were computed using a Fast Fourier Transform with 2,048 points, giving a frequency resolution of 49 Hz. The variance of the pressure fluctuation was calculated by integrating the auto-spectrum. The coherence is defined as the squared modulus of the cross-spectrum normalized by the product of the auto-spectra. In the presentation of the results, time and frequency are non-dimensionalized by the parameter U_e/H_t, where U_e is the ideally-expanded velocity (see Eq. 12) and H_t is the throat height.

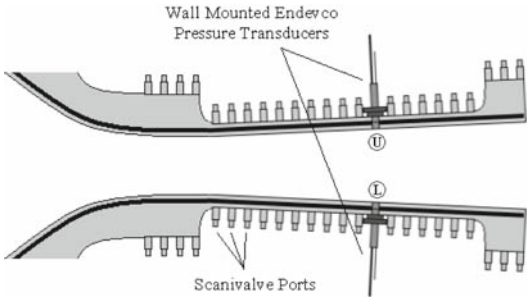

Fig. 5 Installation of transducers for time-resolved wall pressure measurements

3 Results

3.1 Schlieren photography

Spark schlieren photography captured the instantaneous features of the shock system and the ensuing turbulent flow separation. We present in Figs. 6 and 7 the sequence of shock formation with increasing NPR for $A_e/A_t = 1.2$ and 1.5, respectively. For both area ratios, a well-defined shock appears at NPR $= 1.2$. For the lower area ratio, the shock is symmetric and nearly straight for low to moderate NPRs. For NPR > 1.4, the shock acquires symmetric "lambda feet" near the walls. Each lambda foot is characterized by the incident shock, reflected shock, and the triple point where the incident and reflected shocks merge into the Mach stem. A slipstream (entropy layer) originates at each triple point. For $A_e/A_t = 1.5$, lambda feet appear at NPR $= 1.3$ and become progressively larger with increasing NPR. Except at very low value of NPR, the shock structure is asymmetric and exhibits a large lambda foot on one side and a small one on the other side. For $A_e/A_t \geq 1.4$ and NPR > 1.3, we never observed symmetric formation of the shock.

During the duration of a given test, which lasted up to 15 s, the asymmetry of the shock did not change, i.e., the lambda feet did not flip. We verified this by flashing the spark gap at high frequency and recording the images on a video camera (in essence, taking a movie of the flow but

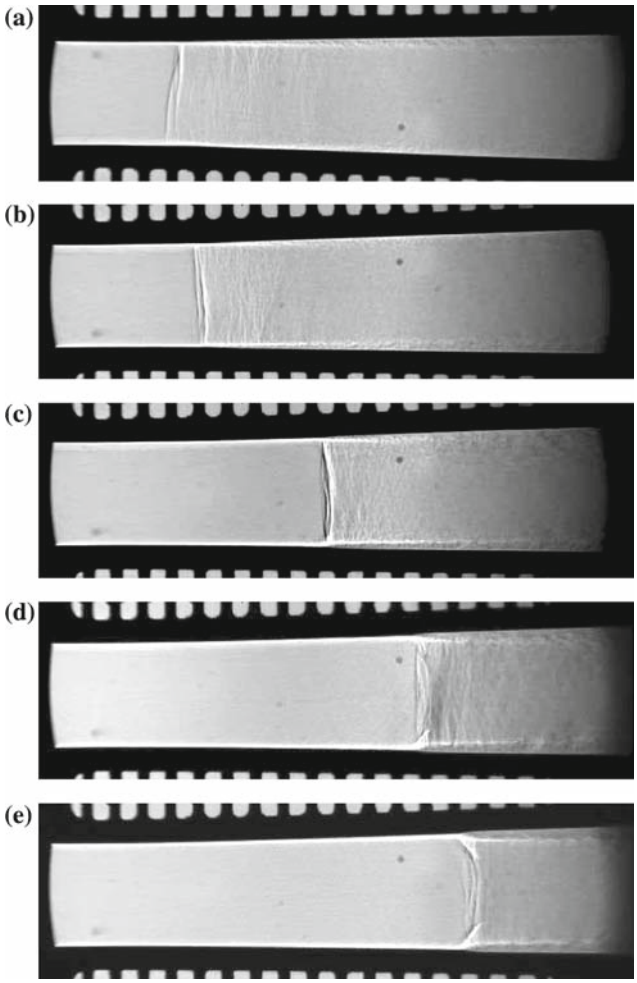

Fig. 6 Schlieren images of shock with increasing nozzle pressure ratio for $A_e/A_t = 1.20$. NPR = **a** 1.20, **b** 1.28, **c** 1.35, **d** 1.40, **e** 1.55

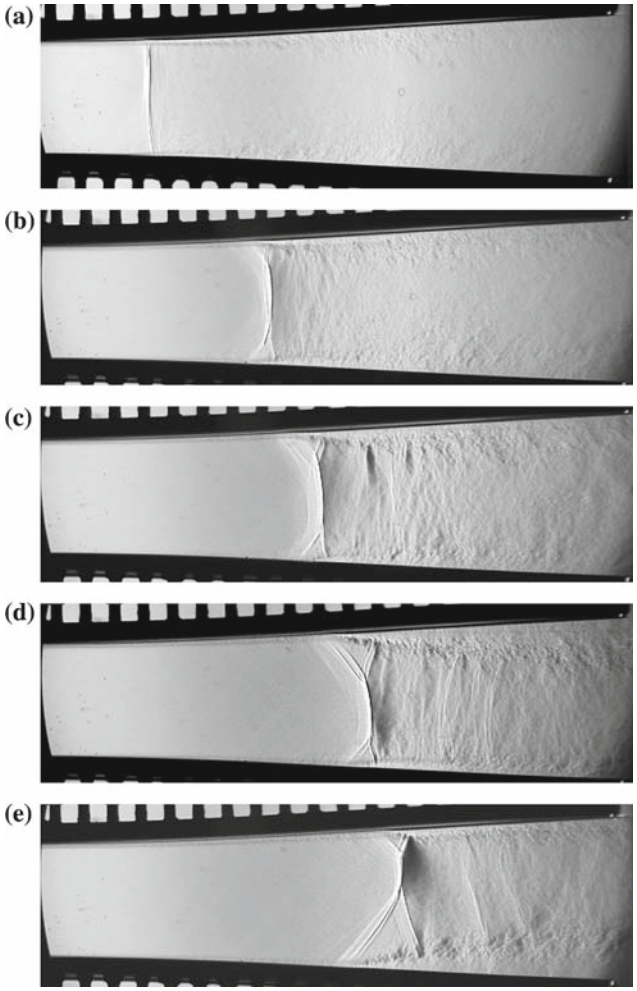

Fig. 7 Schlieren images of shock with increasing nozzle pressure ratio for $A_e/A_t = 1.40$. NPR = **a** 1.20, **b** 1.33, **c** 1.44, **d** 1.59, **e** 1.77

with time-uncorrelated frames). However, when we stopped and restarted the flow, at exactly the same pressure ratio and nozzle geometry, the shock asymmetry could flip. In other words, the shock chooses its orientation at the start-up of the run and retains the same orientation throughout the run. The asymmetry of the flow could be the manifestation of a "Coanda effect" whereby a jet surrounded by or adjacent to a solid surface attaches to the surface. Asymmetric separation in CD nozzles was also observed in the experimental study of Bourgoing and Reijasse [16].

The separation shear layer downstream of the large lambda foot grows rapidly and displays very strong instability. In contrast, the shear layer emerging from the small lambda foot grows at a slow rate. Figure 8 shows details of the shock structure and separated flow. Very large eddies, sometimes occupying more than half the test section height, are seen to emerge downstream of the large lambda foot. For large area ratios, the shock system is unsteady in the axial direction but not exceedingly so. Video realizations indicate that the axial travel distance was on the order of half the local test section height.

Another very important feature of the flow is the succession of weak normal shocks ("aftershocks") past main shock. This phenomenon occurred in all our visualizations but is particularly well captured in the photographs of Fig. 8. The presence of shocks downstream of the main part of the separation shock indicates that flow accelerates to supersonic speed, recompresses, reaccelerates, etc. This means that, immediately downstream of the Mach stem, there is no pressure recovery. Instead, there is an underexpansion. Close examination of Fig. 8 shows expansion fans emanating from the intersection of the reflected shocks with the separation shear layers. Evidently, the reflected shock of the lambda foot is of the "weak" type, i.e., flow downstream of the shock is supersonic. The interaction of the shock with the shear layer is similar to the boundary layer-shock interaction studied by Liepmann [17] in transonic flows over airfoils.

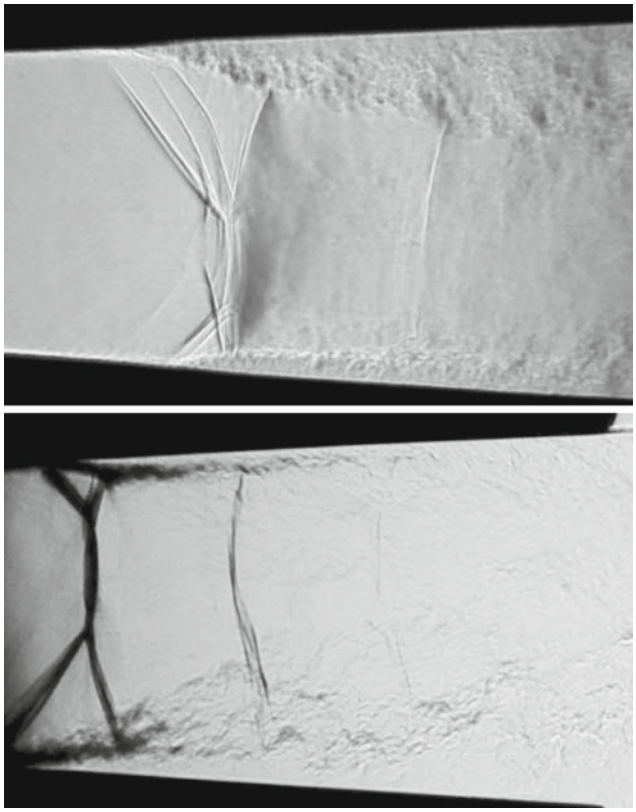

Fig. 8 Details of shock and separated flow for $A_e/A_t = 1.5$ and NPR = 1.5. The two pictures were taken with slightly different illumination settings and fields of view

The presence of shocks spanning the entire jet of the separated flow (not confined to the supersonic region past each lambda foot) indicates that flow downstream of the main shock accelerates to speeds that have locally supersonic values. This must be accomplished by the slipstream forming sonic throat and then diverging. The presence of multiple shocks suggests that, further downstream, the slipstream creates additional sonic throats. Thus, it appears that a "wavy" slipstream is created that supports the alternation of subsonic and supersonic flow. The flow images suggest that the expansion waves emanating from the intersection of the reflected shock with the shear layer are transmitted through the slipstream, which means that the slipstream is supersonic at the position where it is intercepted by the expansion waves. The nearly-straight shape of the aftershocks further suggests that the entire jet acquires a nearly uniform velocity a short distance past the Mach stem. The above observations are summarized in the sketch of Fig. 9 which depicts our present understanding of the principal shock and fluid phenomena. Secondary interactions, such as reflections from the slipstreams, are not shown.

A large number of pictures was processed to obtain the shock position versus area ratio and pressure ratio. Shock position A_s/A_t is defined as the area ratio corresponding

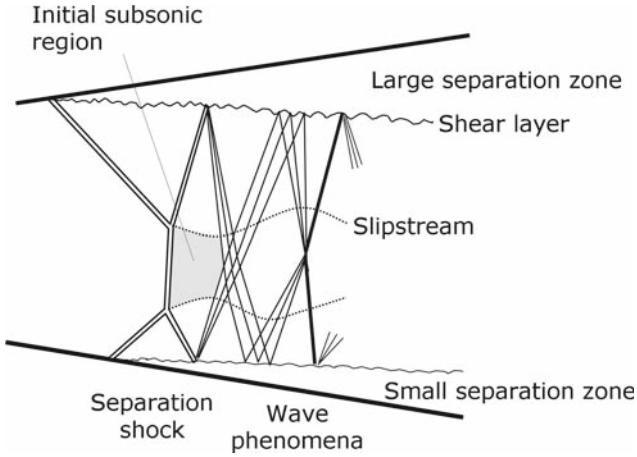

Fig. 9 Conjecture on shock and fluid phenomena

to the axial position of the Mach stem (normal part) of the shock. Figure 10 plots the shock position versus NPR for four nozzle area ratios. Notable is the substantial discrepancy between the actual shock position and the position predicted by one-dimensional inviscid theory. The discrepancy worsens with increasing area ratio. The shock sits at an area ratio much smaller than that predicted by the theory. The physical reason is the the underexpansion, noted above, that forms immediately downstream of the normal shock. The underexpansion creates a "back pressure" much higher than the theory predicts, causing the shock to sit at a smaller than expected area ratio. As mentioned in the introduction, the discrepancy with theory was evident by a few data points collected by previous investigations. We believe, however, that this is the first systematic study of shock location versus area ratio and pressure ratio. Deviation of the shock location data from the best fit curves in Fig. 10 is an indication of shock unsteadiness, which evidently increases with area ratio.

3.2 Wall pressure

Static pressure distributions along the upper wall of the nozzle are plotted in Fig. 11 for various nozzle pressure ratios and three area ratios. Since the nozzle is symmetric, there are no noticeable differences between the upper and lower wall pressure distributions except at large area ratios and large nozzle pressure ratios. The pressure distributions have the "classic" shape of expansion, shock jump, and recovery. The major difference from the theoretical case is that, for a given pressure ratio, the shock Mach number, and therefore the pressure jump, are much smaller.

As mentioned in the previous section, for large A_e/A_t and NPR > 1.4, the shock structure is asymmetric. This creates a small change in the pressure distributions on the upper and lower nozzle surfaces. Figure 12 compares the upper

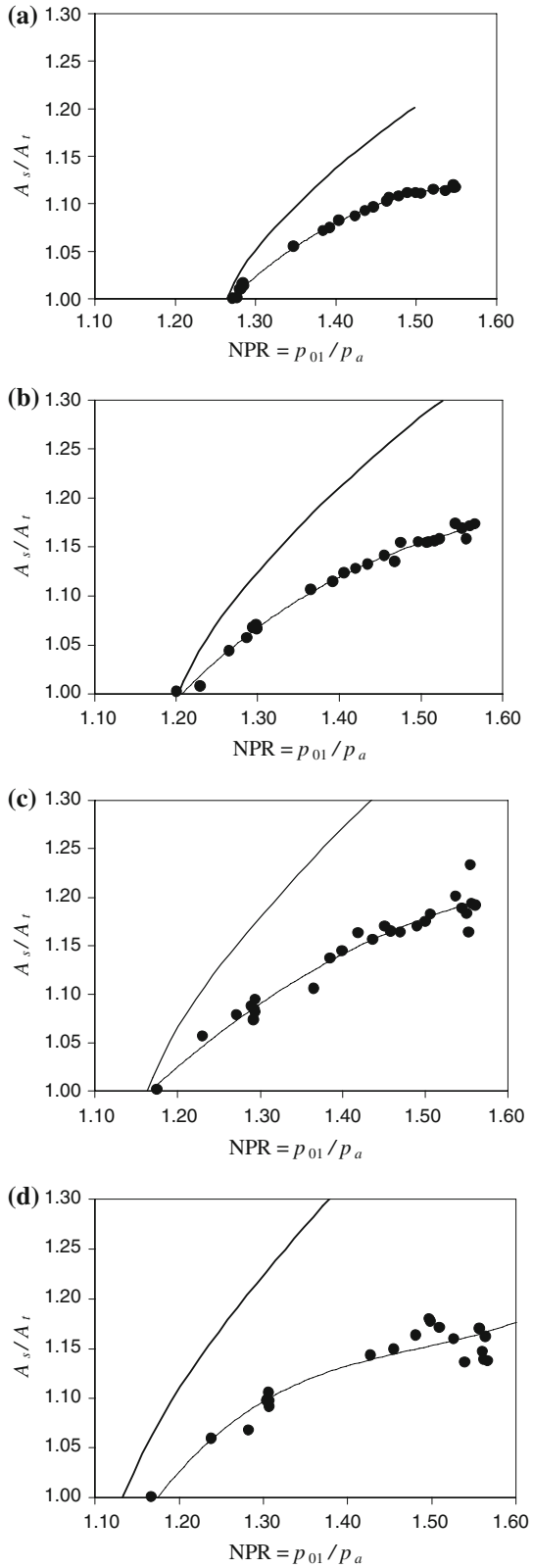

Fig. 10 Shock Location versus NPR for A_e/A_t = **a** 1.20, **b** 1.30, **c** 1.40, **d** 1.50. *Thin line* is best fit of data, *thick line* is prediction of one-dimensional inviscid theory

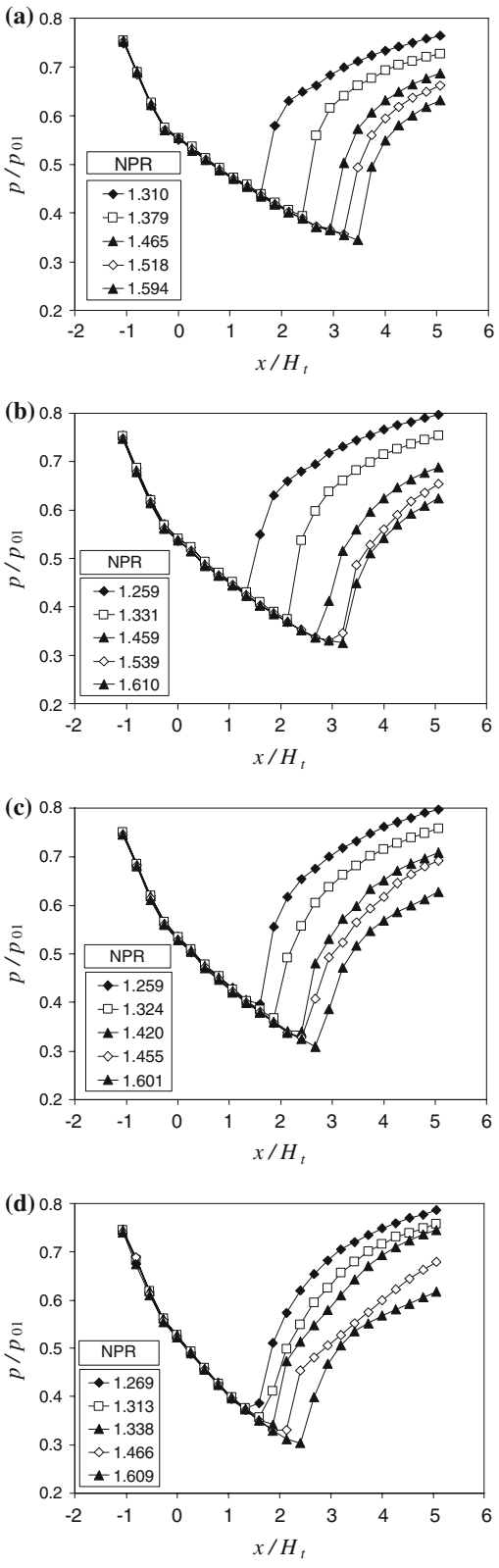

Fig. 11 Static pressure distribution on the upper wall of a nozzle A_e/A_t == **a** 1.20, **b** 1.30, **c** 1.40, **d** 1.50

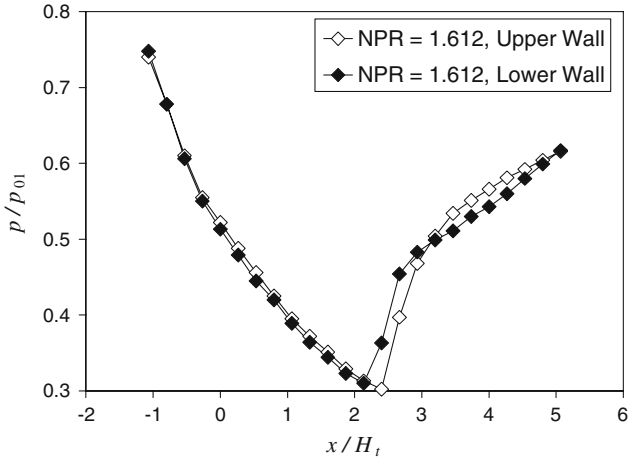

Fig. 12 Static pressure distributions on the upper and lower walls of the nozzle

and lower wall pressure distributions for $A_e/A_t = 1.5$ and NPR $= 1.61$. There is a distinct difference in the pressure recovery past the shock. On the side of the large lambda foot (lower wall), pressure recovers linearly with distance. This type of recovery is similar to the "strong-shock" recovery in diffusers measured by Sajben et al. [18] and predicted numerically by Xiao et al. [19]. On the side of the small lambda foot (upper wall), the pressure shows a faster initial rise followed by a gradual recovery to ambient value. The asymmetric recovery creates a small sideward force on the nozzle, which we calculate to be around 1–2% of the nozzle thrust. It is important to note that the wall pressure past the separation shock does not adjust to the ambient pressure immediately. Although an immediate pressure adjustment occurs in large-area-ratio nozzles, in nozzles with small to moderate pressure ratio the adjustment is gradual. This means that Romine's theory [10], which assumes immediate recovery, is not applicable here unless the shock sits at the nozzle exit.

3.3 Centerline pressure

Figure 13 plots the centerline static pressure distribution, measured with the translating tube of Fig. 4, for various area ratios and nozzle pressure ratios. The trends are similar to those for the wall pressure, except that the "recovery" past the shock has a different shape. For NPR > 1.5 the pressure past the shock shows a flat region, or a slight dip, followed by a gradual rise to the ambient value. A direct comparison between wall and centerline pressures is shown in Fig. 14. The pressure rise on the centerline is sharper than that on the walls. The pressure dip that follows is qualitatively consistent with the conjecture of Fig. 9. However, the quantitative behavior in the vicinity of the shock was surprising at first.

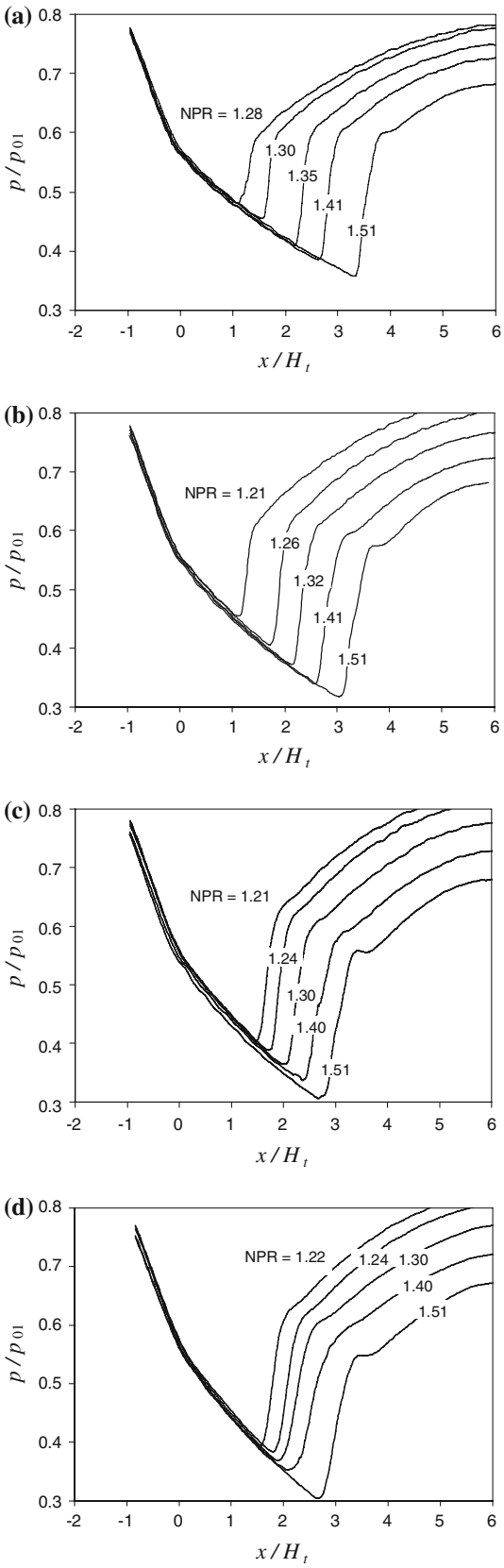

Fig. 13 Centerline pressure distribution versus NPR for A_e/A_t == **a** 1.20, **b** 1.30, **c** 1.40, **d** 1.50

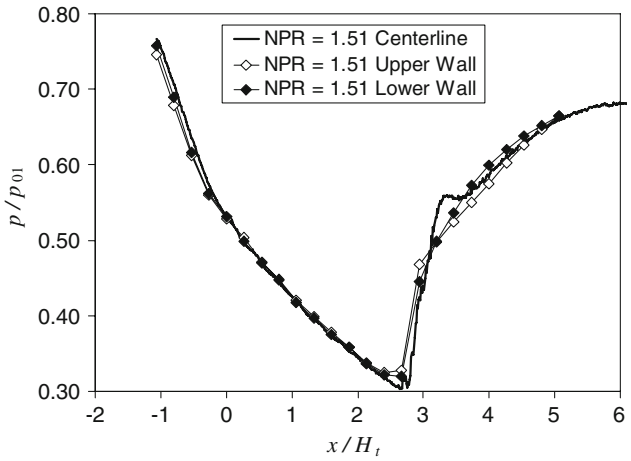

Fig. 14 Comparison of wall versus centerline pressure distribution for $A_e/A_t = 1.4$

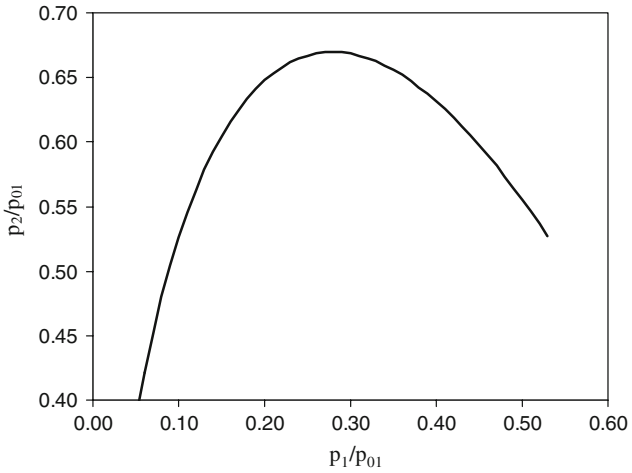

Fig. 15 Normal shock relation for static pressure before and after the shock

In contrast to the complex shock structure near the wall, the shock near the nozzle centerline is a clean normal shock. We thus expect the pressure rise across the shock to follow the normal-shock relation

$$\frac{p_2}{p_1} = 1 + \frac{2\gamma}{\gamma+1}(M_1^2 - 1) \tag{1}$$

where M_1 is the flow Mach number immediately upstream of the shock and is related to the local static pressure p_1 via

$$\frac{p_1}{p_{0_1}} = \left(1 + \frac{\gamma-1}{2}M_1^2\right)^{\frac{-\gamma}{\gamma-1}} \tag{2}$$

Combining Eqs. 1 and 2 we arrive at a relation of p_2 versus solely p_1,

$$\frac{p_2}{p_{0_1}} = \frac{4\gamma}{\gamma^2-1}\left(\frac{p_1}{p_{0_1}}\right)^{\frac{1}{\gamma}} - \frac{(\gamma+1)^2}{\gamma^2-1}\frac{p_1}{p_{0_1}} \tag{3}$$

which is plotted in Fig. 15. It is evident from the centerline-pressure plot of Fig. 14 that the measured pressure rise across the shock does not satisfy Eq. 3. To clarify this point, we plot in Fig. 16a the centerline pressure distribution for $A_e/A_t = 1.5$ and NPR = 1.61. Just before the shock, we have $p_1/p_{0_1} = 0.30$. The peak pressure of the shock is $p/p_{0_1} = 0.55$, much less than the normal-shock solution $p_2/p_{0_1} = 0.67$. One could argue that, since the shock is unsteady, the steady normal shock relations may not hold. Since we do not know the details of the shock motion (it is not harmonic, as will be shown later), we cannot fully answer this point. On the other hand, we can make the simple argument that a velocity u_s of the shock relative to a stationary observer should increase the time-averaged pressure ratio: the shock Mach number becomes $M_s = M_1 + u_s/a_1$ and the pressure ratio depends on the square of the shock Mach number. Moreover, we know from the visualizations that flow past the shock undergoes a substantial expansion that is not shown in the measurements. So the behavior of the centerline pressure distribution cannot be explained by a possible effect of unsteadiness on the normal shock relations.

It will now be shown that the shape of the centerline pressure distribution is likely the result of smoothing due to the shock motion. The centerline probe does not measure the true pressure distribution but a filtered distribution, which can be expressed as the convolution of the true pressure $p(x)$ with a response function $r(x)$

$$p_{\text{meas}}(x) = \int p(\xi)\, r(x-\xi)\mathrm{d}\xi \tag{4}$$

For the response function we assume a Gaussian kernel

$$r(x) = \frac{1}{b\sqrt{\pi}}e^{-(x/b)^2} \tag{5}$$

Evaluation of Eq. 4 was done using Fourier transforms. The pressure distribution of Fig. 16a was reshaped into a hypothetical distribution, shown in Fig. 16b, having a nearly discontinuous pressure jump that satisfies the normal shock relations. The shock of this hypothetical curve was placed in the middle of the shock rise of the measured pressure distribution. The pressure before the shock was calculated by extrapolating linearly the measured data upstream of the shock to the shock location, resulting in $p_1/p_{0_1} = 0.27$. The pressure jump is followed by a rapid expansion that brings the pressure down to the level of the small plateau that forms past the shock in the measured data.

Figure 16b shows the result of smoothing of the hypothetical pressure distribution with a Gaussian kernel having full-width $2b = 13$ mm. The smoothed curve and the actual curve of Fig. 16a practically coincide. The Gaussian full-width is about one half of the test section height, which agrees with our visual observation of shock motion. Of course, the hypothetical curve of Fig. 16b is not unique and this

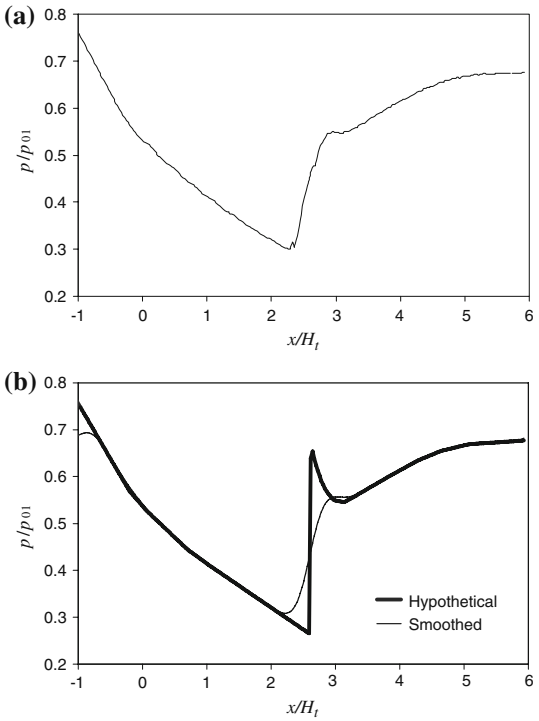

Fig. 16 Centerline pressure distribution for $A_e/A_t = 1.4$ and NPR = 1.5. **a** Actual, **b** hypothetical without and with Gaussian smoothing

exercise is neither a rigorous nor a perfect reconstruction of the true pressure distribution. Using sophisticated deconvolution methods one may be able to recover the true pressure distribution without any assumptions, but the numerical challenges are significant. What we have shown here is that the measured pressure distributions is consistent with Gaussian smoothing of a pressure distribution that satisfies the normal shock relations.

Importantly, the hypothetical curve of Fig. 16b clarifies the flow process in the vicinity of the nozzle centerline for the conditions examined in this experiment. Instead of a monotonic adjustment to the ambient pressure, we have expansion followed by compression. We already observed in the flow visualizations that the expansion results from the reflection of the reflected shock of the lambda foot from the shear layer of the separation zone. As long as the reflected shock is of the "weak" type (i.e., the outflow is supersonic), an expansion is inevitable. Flow past the the Mach stem needs to adjust to this lower pressure, therefore it also accelerates to supersonic speed, as illustrated by Fig. 9. The expansion brings the pressure to a level below ambient, thus a compression is needed for matching the ambient pressure. In the above discussion we attributed smoothing of the centerline pressure distribution to the motion of the shock. Additional smoothing, but probably of lesser extent, may be caused by the interaction of the shock with the boundary layer of the probe.

3.4 Time-resolved wall pressure measurements

Time-resolved wall pressure measurements, using the probe arrangement of Fig. 5, were used to infer quantitative information on the motion of the shock and the turbulence fluctuations before and after the shock. To measure the wall pressure fluctuations in the entire neighborhood of the shock, the nozzle was held at a fixed area ratio of $A_e/A_t = 1.6$ and the nozzle pressure ratio was gradually increased pushing the shock from upstream to downstream of the probe location. Figure 17 shows the variation of rms wall pressure fluctuation of one of the two probes, p'_{rms}, with nozzle pressure ratio. At higher NPR, when the shock is downstream of the probe, the probe measures very weak pressure fluctuations associated with the attached boundary layer. As the NPR is lowered and the shock is positioned over the probe, the probe measures very intense pressure fluctuations associated with the motion of the shock. At even lower NPR, when the probe senses the separated region, the fluctuations are larger than in the attached boundary layer but smaller than when the shock is over the probe.

Figure 18 plots the auto-spectra corresponding to the three regimes of Fig. 17. The spectrum of the fluctuations in the attached boundary layer is significantly lower in intensity than the spectra in the two other regimes. It is reasonable to assume that the attached boundary layer plays little or no role on the shock motion. The spectrum of pressure fluctuations in the "shock" regime is broadband without any discrete tones. The same holds for the spectrum in the "separation" region which has similar shape, but lower level, than the spectrum in the "shock" region. The spectra of Fig. 18 are similar to the corresponding spectra of shock-boundary layer separation in front of a wedge studied by Plotkin [20].

We now examine the cross-correlation and coherence of the lower and upper wall proves (Fig. 5) for the three regimes of Fig. 17. The cross correlation plots of Fig. 19a show lack

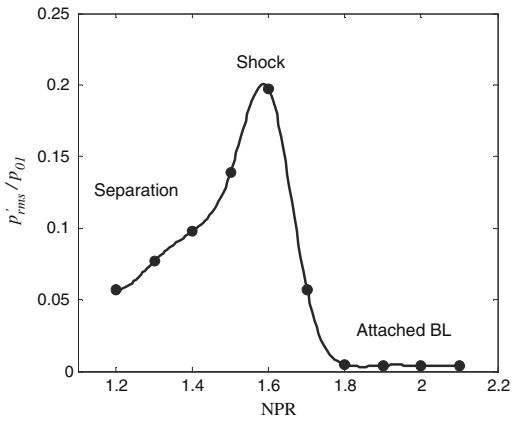

Fig. 17 RMS wall static pressure fluctuation versus nozzle pressure ratio, showing different flow regimes

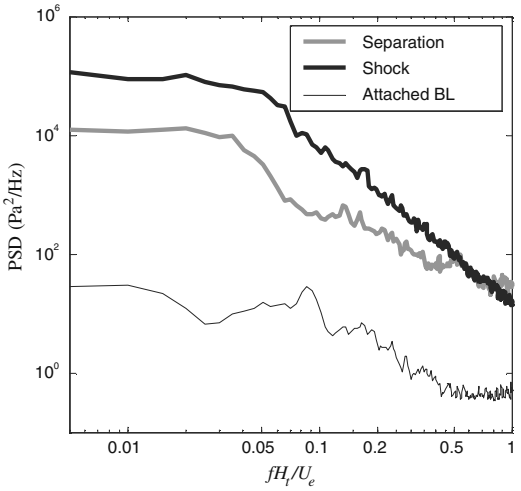

Fig. 18 Autospectra of wall static pressure corresponding to the various flow regimes

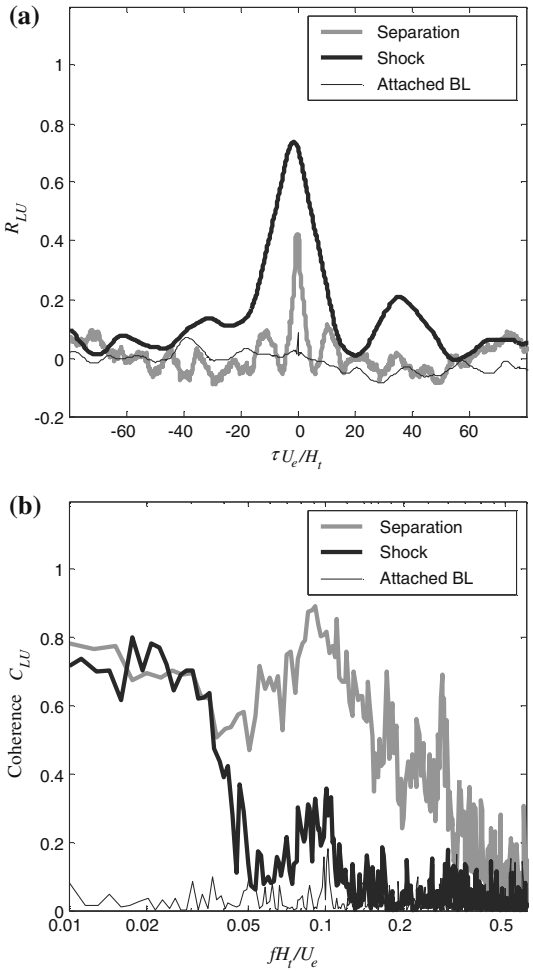

Fig. 19 **a** Cross correlation and **b** coherence of the upper and lower wall static ports

of correlation in the attached boundary layer, very strong correlation when the shock is over the probes, and significant correlation in the separated flow region. Importantly, the cross-correlations for both the "shock" and "separation" regions peak at $\tau = 0$, indicating no significant time lag between the motion of the upper and lower portions of the shock and the respective downstream pressure fluctuations. In other words, the shock oscillates in a piston-like motion and creates a transversely coherent pressure wave sensed downstream of the shock. The coherence plots of Fig. 19b provide information on the frequency content of the aforementioned cross-correlations. When the probes sense the attached boundary layer the coherence of the two probes is practically zero, which is indicative of random turbulent eddies on each wall. When the shock is over the probes, the coherence is very strong at low frequency and declines rapidly for $fH_t/U_e > 0.05$. This indicates that the transversely-coherent part of the shock motion is a low-frequency phenomenon. In the separated region downstream of the shock, the coherence of the two probes covers a broader frequency band. It practically coincides with the coherence in the "shock" region for $0 < fH_t/U_e < 0.05$ and remains significant up to $fH_t/U_e = 0.5$. This suggests the generation of a higher-frequency (smaller-wavelength) pressure wave system that is coherent across the entire nozzle height. Such system could be associated with the succession of shock and expansion waves depicted in Fig. 9.

3.5 Thrust

Given that one of the intended applications of the mixing enhancement phenomenon is on aeroengines, it is important to assess the thrust loss caused by flow separation inside a convergent–divergent nozzle. From the preceding results it is clear that one-dimensional theory would be very inadequate for thrust prediction. This experiment has generated results—the wall pressure distributions—that allow an estimate of thrust loss. This estimate will not include shear stresses; however, their impact is much smaller than the impact of the pressure distribution created by the shock.

The procedure for calculating thrust is explained in Fig. 20. For simplicity, and without loss of generality, we consider a "half nozzle." The ideal thrust is created by the "design" nozzle for given NPR. Specifically, the design nozzle it is a nozzle with the same NPR and mass flow rate as the actual nozzle, that produces a shock-free flow with pressure-matched exhaust. For subcritical nozzle pressure ratios (NPR < 1.893 for $\gamma = 1.4$), the shape of the design nozzle is convergent. With respect to the full nozzle shown in Fig. 20a, the design nozzle comprises the portion of the nozzle upstream of the design point "d" where $p = p_a$. The resulting nozzle, shown in Fig. 20b, has the same NPR and same mass flow rate as the actual nozzle.

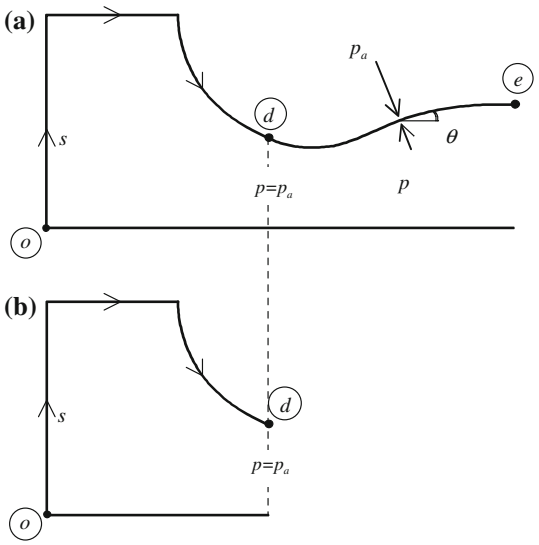

Fig. 20 Procedure for calculating thrust of **a** actual nozzle and **b** ideal nozzle

The thrust of a nozzle equals the integral of the axial components of the forces acting on the internal and external walls of the nozzle and supply reservoir. Here we deal only with pressure forces. At static conditions, the external pressure is ambient, p_a. A portion of the internal pressure distribution p (from a short distance upstream of the nozzle throat to the nozzle exit) is known from our measurements. Letting s denote the coordinate along the surface of the nozzle and θ the local angle of the surface, the thrust of the actual nozzle is

$$F = \int_o^e (p - p_a) \sin\theta \mathrm{d}s \tag{6}$$

The thrust integral can be divided into two parts, the contribution upstream of the design point and the contribution downstream of the design point:

$$F = \int_o^d (p - p_a) \sin\theta \mathrm{d}s + \int_d^e (p - p_a) \sin\theta \mathrm{d}s \tag{7}$$

The first integral represents the ideal thrust, which equals the momentum flux of the perfectly expanded flow:

$$F_i = \int_o^d (p - p_a) \sin\theta \mathrm{d}s = \dot{m} U_e \tag{8}$$

where $\dot{m}$ is the mass flow rate and U_d is the design (perfectly-expanded) velocity. Therefore the actual thrust is

$$F = \dot{m} U_e + \int_d^e (p - p_a) \sin\theta \mathrm{d}s \tag{9}$$

and the thrust coefficient is

$$\frac{F}{F_i} = 1 + \frac{1}{\dot{m} U_e} \int_d^e (p - p_a) \sin\theta \mathrm{d}s \tag{10}$$

The mass flow rate is based on the sonic conditions in the actual nozzle,

$$\dot{m} = A_t \gamma \frac{p_{0_1}}{a_0} \left(\frac{\gamma + 1}{2} \right)^{\frac{\gamma+1}{1-\gamma}} \tag{11}$$

where $a_0 = \sqrt{\gamma R T_0}$ is the reservoir speed of sound. The fully-expanded velocity is given by the relation

$$U_e = a_0 \sqrt{\frac{2}{\gamma - 1} \left(1 - \mathrm{NPR}^{(1-\gamma)/\gamma}\right)} \tag{12}$$

Integration of the pressure started at the point "d", where $p = p_a$, and ended at the nozzle exit. For NPR < 1.35, point "d" was located upstream of the first static pressure port, therefore it could not be resolved. For this reason, the thrust calculation was performed for NPR > 1.35.

Figure 21 shows the thrust coefficient versus NPR for various nozzle area ratios. For $A_e/A_t < 1.5$, the thrust coefficient drops then rises with increasing NPR. For $A_e/A_t = 1.5$ the thrust coefficient is seen to rise monotonically with NPR, although it is possible that a minimum occurs at NPR < 1.35. As expected, the thrust coefficient drops with increasing area ratio, a consequence of stronger shocks and higher total pressure loss. The overall trends and values are consistent with those of past works that measured nozzle thrust directly [6,9]. It is important to note that in many envisioned applications, such as military engines, the thrust allocated to mixing enhancement would be on the order of 10–20% of the total engine thrust [3]. Thus, a loss of 7% in the thrust of the secondary flow used for mixing enhancement translates to a thrust loss on the order of 1% for the entire engine.

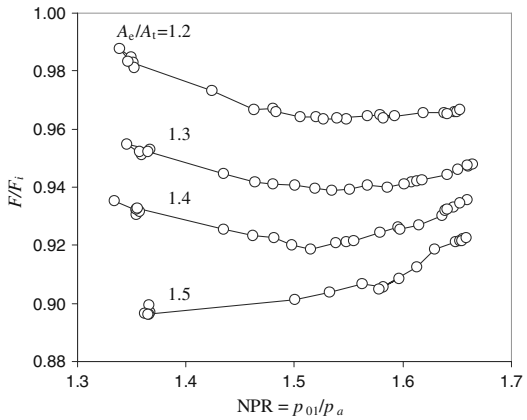

Fig. 21 Thrust coefficient versus NPR for various area ratios

4 Concluding remarks

We conducted an experimental study of supersonic flow separation in a planar converging-diverging nozzle with flexible geometry and variable pressure ratio. The range of flow conditions was $1.0 < A_e/A_t < 1.6$ and $1.2 < \mathrm{NPR} < 1.8$. We summarize our findings as follows.

For $A_e/A_t > 1.2$ and NPR > 1.4, the separation shock has a well-defined lambda shape. For large values of A_e/A_t and NPR, one lambda foot is always larger than the other, i.e., separation occurs asymmetrically. The asymmetry does not flip during a given test run, but can change side from run to run. The occurrence of the asymmetric separation lambda shock is consistent with past observations in nozzles with large area ratio [16]. Flow downstream of the Mach stem accelerates rapidly to supersonic speed by means of expansion waves created by the reflection of the trailing shock of the lambda foot from the separation pressure boundary. Visualization of flow past the Mach stem shows a series of weak normal shocks across the entire separated flow, indicating successive expansions and compressions of the separated flow.

A systematic visual study of shock position versus NPR and A_e/A_t indicates that the shock sits at an area smaller (closer to the throat) than the prediction of quasi-one-dimensional theory. This is explained by the larger "back-pressure" associated with aforementioned expansion past the Mach stem. The departure from theory is aggravated as the nozzle area ratio increases. With increasing NPR and A_e/A_t, instantaneous visualizations indicate that the shock becomes progressively more unsteady and the range of its axial motion is approximately one half of the local test section height. The shock motion smooths out the centerline pressure distribution measured by a static pressure probe, thereby obliterating critical features of the true pressure distribution.

Time-resolved wall pressure measurements indicate that the shock motion has strong coherence across the nozzle height, indicating that the shock pulsates in a piston-like manner. The wall-pressure field immediately past the shock exhibits the same type of transverse coherence. The spectrum of the wall pressure directly influenced by the shock indicates that the shock motion is a low-frequency phenomenon. For the dimensions and Reynolds numbers of this study, the shock motion was not harmonic.

The separation shear layer on the side of the large lambda foot exhibits intense instability that grows into very large eddies at the nozzle exit. The shear layer on the side of the small lambda foot grows normally. Thus, the mixing enhancement phenomenon that motivated this study appears to be strongly connected with asymmetric flow separation and could also be influenced by the succession of compression and expansion waves that follow the main separation shock.

Acknowledgments We are grateful for the support by the National Science Foundation (Grant No. CTS-0072964), NASA Glenn Research Center (Grant NAG-3-2345 monitored by Dr. Khairul B. Zaman), and the National University of Singapore (Contract No. TL/AE/2004/0001, monitored by Dr. Her Mann Tsai).

References

1. Papamoschou, D.: Mixing enhancement using axial flow. AIAA Paper 2000-0093 (2000)
2. Murakami, E., Papamoschou, D.: Experiments on mixing enhancement in dual-stream jets. AIAA Paper 2001-0668 (2001)
3. Papamoschou, D., Dixon, T.D., Nishi, K.: Mean flow of multi-stream rectangular jets under normal and mixing-enhancement conditions, AIAA Paper 2004-0919 (2004)
4. Morrisette, E.L., Goldberg, T.J.: Turbulent flow separation criteria for overexpanded supersonic nozzle. NASA TP 1207 (1978)
5. Reshotko, E., Tucker, M.: Effect of a discontinuity on turbulent boundary layer thickness parameters with application to shock-induced separation. NACA TN-3454 (1955)
6. Wilmoth, R.G., Leavitt, L.D.: Navier Stokes predictions of multi-function nozzle flows. SAE Trans. **96**(6), 6.865–6.879 (1987)
7. Hamed, A., Vogiatzis, C.: Overexpanded two-dimensional convergent-divergent nozzle flow simulations, Assessment of Turbulence Models. J. Propulsion Power **13**(3), 444–445 (1997)
8. Hamed, A., Vogiatzis, C.: Overexpanded two-dimensional convergent-divergent nozzle flow performance, effects of three-dimensional flow interactions. J. Propulsion Power **14**(2), 234–440 (1998)
9. Hunter, C.A.: Experimental, theoretical and computational investigation of separated nozzle flows. AIAA Paper 98-3107 (1998)
10. Romine, G.L.: Nozzle flow separation. AIAA J. **36**(9), 1618–1625 (1998)
11. Zaman, K.B.M.Q., Dahl, M.D., Bencic, T.J., Loh, C.Y.: Investigation of a transonic resonance with convergent-divergent nozzles. J. Fluid Mech. **263**, 313–343 (2002)
12. Zaman, K.B.M.Q, Papamoschou, D.: Study of mixing enhancement observed with a co-annular nozzle configuration. AIAA Paper 2000-0094 (2000)
13. Papamoschou, D., Zill, A.: Fundamental investigation of supersonic nozzle flow separation. AIAA Paper 2004-1111 (2004)
14. Papamoschou, D., Johnson, A.: Unsteady phenomena in supersonic nozzle flow separation. AIAA Paper 2006-3360 (2006)
15. Anderson, J.D.: Modern Compresible Flow. McGraw Hill, New York (1990)
16. Bourgoing, A., Reijasse, Ph.: Experimental analysis of unsteady separated flows in a supersonic planar nozzle. Shock Waves **14**(4), 251–258 (2005)
17. Liepmann, H.W.: The interaction between boundary layer and shock waves in transonic flow. J. Aero. Sci. **13**(12), 623–637 (1946)
18. Sajben, M., Bogar, T.J., Kroutil, J.C.: Characteristic frequencies of transonic diffuser flow oscillations. AIAA J. **21**(9), 1232–1240 (1983)
19. Xiao, Q., Tsai, H.M., Liu, F.: Computation of transonic diffuser flows by a legged $k-\omega$ turbulence model. AIAA J. **19**(3), 473–483 (2003)
20. Plotkin, K.J.: Shock wave oscillation driven by turbulent boundary-layer fluctuations. AIAA J. **13**(8), 1036–1040 (1975)